This paper is published as part of a PCCP Themed Issue on:
Metal oxide nanostructures: synthesis, properties and applications

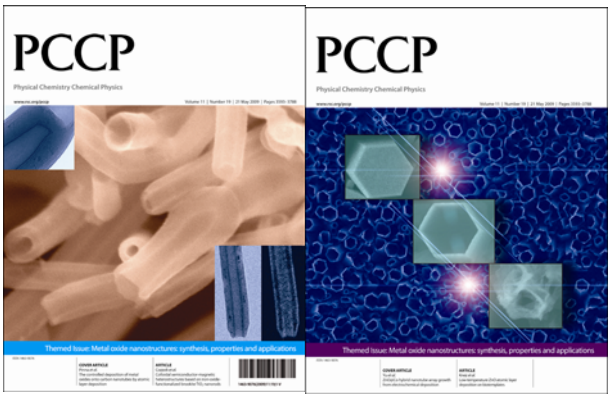

Guest Editors: Nicola Pinna, Markus Niederberger, John Martin Gregg and Jean-Francois Hochepied

Editorial

Papers

Thin-walled Er^{3+}:Y_2O_3 nanotubes showing up-converted fluorescence
Christoph Erk, Sofia Martin Caba, Holger Lange, Stefan Werner, Christian Thomsen, Martin Steinhart, Andreas Berger and Sabine Schlecht, *Phys. Chem. Chem. Phys.*, 2009
DOI: 10.1039/b821304f

Wettability conversion of colloidal TiO_2 nanocrystal thin films with UV-switchable hydrophilicity
Gianvito Caputo, Roberto Cingolani, Pantaleo Davide Cozzoli and Athanassia Athanassiou, *Phys. Chem. Chem. Phys.*, 2009
DOI: 10.1039/b823331d

Nucleation and growth of atomic layer deposition of HfO_2 gate dielectric layers on silicon oxide: a multiscale modelling investigation
A. Dkhissi, G. Mazaleyrat, A. Estève and M. Djafari Rouhani, *Phys. Chem. Chem. Phys.*, 2009
DOI: 10.1039/b821502b

Designing meso- and macropore architectures in hybrid organic–inorganic membranes by combining surfactant and breath figure templating (BFT)
Ozlem Sel, Christel Laberty-Robert, Thierry Azais and Clément Sanchez, *Phys. Chem. Chem. Phys.*, 2009
DOI: 10.1039/b821506e

The controlled deposition of metal oxides onto carbon nanotubes by atomic layer deposition: examples and a case study on the application of V_2O_4 coated nanotubes in gas sensing
Marc-Georg Willinger, Giovanni Neri, Anna Bonavita, Giuseppe Micali, Erwan Rauwel, Tobias Herntrich and Nicola Pinna, *Phys. Chem. Chem. Phys.*, 2009
DOI: 10.1039/b821555c

***In situ* investigation of molecular kinetics and particle formation of water-dispersible titania nanocrystals**
G. Garnweitner and C. Grote, *Phys. Chem. Chem. Phys.*, 2009
DOI: 10.1039/b821973g

Chemoresistive sensing of light alkanes with SnO_2 nanocrystals: a DFT-based insight
Mauro Epifani, J. Daniel Prades, Elisabetta Comini, Albert Cirera, Pietro Siciliano, Guido Faglia and Joan R. Morante, *Phys. Chem. Chem. Phys.*, 2009
DOI: 10.1039/b820665a

Electrochemistry of $LiMn_2O_4$ nanoparticles made by flame spray pyrolysis

T. J. Patey,[ab] R. Büchel,[c] M. Nakayama[b] and P. Novák*[a]

Received 1st December 2008, Accepted 4th March 2009
First published as an Advance Article on the web 25th March 2009
DOI: 10.1039/b821572n

Crystalline $LiMn_2O_4$ nanoparticles with specific surface areas between 53.9 and 203.4 $m^2\ g^{-1}$ (particle size of 25.9–6.9 nm) were produced in a one-step flame spray pyrolysis process by varying the specific combustion enthalpy. An optimized nano-sized powder retained the highest galvanostatic discharge capacity of over 80 mAh g^{-1} beyond 60 cycles at 50 C, a suitable positive material for high power Li-ion batteries. Due to the increase in specific surface area, nanoparticles have the advantages of decreased diffusion path lengths and improved charge transfer, however, it is seen in this work that the lack of crystalline bulk present in $LiMn_2O_4$ nanoparticles less than 15 nm in size does not justify the advantages of higher specific surface area between the current densities of 0.5–50 C.

1. Introduction

Lithium–ion (Li–ion) technology offers the greatest development potential for electric vehicles and advanced energy storage of clean electricity, but increased power density is desired for high power applications.[1] Power density can be increased by selecting positive and negative materials which lead to a higher voltage and also by increasing overall charge/discharge rates. Selecting $LiMn_2O_4$ rather than $LiCoO_2$ as a positive material leads to a higher electrochemical potential *vs.* graphite and is also safer and cheaper.[2–5] Replacing the conventional microparticles of the positive electrode material with nanoparticles significantly increases the electrode/electrolyte interface area, which improves overall charge/discharge rates.[6] Several methods to produce $LiMn_2O_4$ nanoparticles have therefore been investigated.[7–10]

One attractive route to synthesize $LiMn_2O_4$ nanoparticles is flame spray pyrolysis (FSP).[9] FSP has been used to make other positive electrode materials for Li–ion batteries such as $LiCoO_2$[11] and LiV_3O_8.[12] It is a rapid, efficient, and an industrially-scalable route to synthesize oxide nanoparticles. Production rate, flame temperature, flame residence time of particles can be adjusted to control particle growth and morphology.[13] From a process perspective, FSP is attractive to produce $LiMn_2O_4$ nanoparticles continuously in one single step[9] and can include simultaneously carbon synthesis on the surface of the $LiMn_2O_4$ nanoparticles to improve the electronic conductivity and, thus, the overall reaction rate.[10] Recently, we provided an initial overview of the production capabilities of $LiMn_2O_4$ nanoparticles by FSP,[9] however, the electrochemical performance as a function of particle size was not presented.

In this work, specific combustion enthalpy was varied to make $LiMn_2O_4$ nanoparticles with specific surface area (SSA) ranging from 54–203 $m^2\ g^{-1}$. The electrochemical behaviours of the $LiMn_2O_4$ nanoparticles are investigated by cyclic voltammetry. The potential impact of these as-prepared $LiMn_2O_4$ nanoparticles on high power Li–ion batteries is investigated through rate capability experiments.

2. Experimental

The precursor with a Li–Mn ratio of 1 : 2 was prepared by mixing 30.0 g of Mn(III)-acetylacetonate (Aldrich) and 4.5 g of Li-acetylacetonate (Aldrich) into 200 mL of 2-ethylhexanoic acid (Riedel-de Haën) and 100 mL of toluene (Aldrich). The experimental set-up of FSP is described elsewhere in literature.[14] The as-prepared precursor mixture was injected by a syringe pump into the nozzle at a constant feed rate of 3–9 mL min^{-1} as described elsewhere.[15] The precursor solution was dispersed by 1–7 L min^{-1} of oxygen to form a fine spray while a pressure drop of 1.5 bar was maintained across the nozzle tip. For one production batch, a sheath gas of 10 L min^{-1} of oxygen was used. The variation of both precursor injection rate and the oxygen dispersion gas influenced the precursor droplet size, specific combustion enthalpy, and flame length. The spray was ignited by a support flame created by 1 L min^{-1} of methane and 2 L min^{-1} of oxygen. The spray flame nozzle was cooled by water to prevent overheating and precursor evaporation within the liquid feed lines.

In this work, the specific combustion enthalpy (SCE, kJ L_{disp}^{-1}) is defined as the combustion enthalpy of the liquid precursor injection rate in kJ min^{-1} divided by the O_2 dispersion rate in L min^{-1}.[13] The SCE is the most important parameter influencing the particle size, however, additional parameters must be kept constant as for example the molar metal concentration in the precursor.[16]

Particles were collected on a glass-fiber filter (GF/D Whatman, 257 mm in diameter) placed directly over the flame

[a] *Electrochemistry Laboratory, Paul Scherrer Institut, CH-5232, Villigen PSI, Switzerland. E-mail: petr.novak@psi.ch; Fax: +41 56 310 4415; Tel: +41 56 310 2457*
[b] *Department of Applied Chemistry, Tokyo Institute of Technology, Ookayama, Meguro-ku, 152-8552, Tokyo, Japan*
[c] *Particle Technology Laboratory, Department of Mechanical and Process Engineering, ETH Zurich, Sonneggstrasse 3, ML F13, CH-8092, Zurich, Switzerland*

using a vacuum pump (Busch, Seco SV 1025). Adsorbed water was removed from the powders at 150 °C in flowing nitrogen for 90 min at atmospheric pressure before specific surface area (SSA) measurements determined by five-point nitrogen adsorption isotherm at 77 K (Tristar, Micrometrics Instruments Corp.) according to the BET method.[17] The X-ray diffraction (XRD) measurements were performed using a Bruker AXS D8 Advance (40 kV, 40 mA) and analyzed with the Topas 3 software. The XRD measurement was performed at a continuous scan between 2θ angles of 10 and 70° at a scan rate of 0.03° min^{-1}. The crystal sizes, d_{XRD}, were calculated based on the fundamental parameter approach and the Rietveld method.[18]

The same precursor batch was used and flame conditions were varied to make a range of $LiMn_2O_4$ powders (LMO): LMO-3/7, LMO-5/5, LMO-6/4, LMO-7/3, LMO-8/2 and LMO-9/1. For these powder names, the first number refers to the precursor injection rate (mL min^{-1}) and the second to the oxygen dispersion rate (mL L^{-1}). The powder made with an oxygen sheath gas of 10 L min^{-1} during synthesis is referred to as LMO-6/4/10. All powders were prepared in a single step and analyzed as prepared. A commercial $LiMn_2O_4$ powder (Sigma-Aldrich) was also studied in this work.

Electrodes were made from the flame-produced $LiMn_2O_4$ nanoparticles, Super P (commercial carbon black, TIMCAL SA, SSA = 62 m^2 g^{-1}), and polyvinylidene fluoride (PVDF; SOLEF 1015, Solvay) with a mass ratio of 7 : 2 : 1, respectively. Each batch of $LiMn_2O_4$ nanoparticles was mixed with the Super P in *N*-methylpyrrolidinone (NMP; Fluka) solvent and then subsequently with PVDF dissolved in NMP to form a viscous slurry. The slurries were spread at a thickness of 200 μm across aluminum foil and dried under vacuum at 110 °C overnight to remove the NMP and form a working electrode.

Working electrodes 13 mm in diameter were dried in a vacuum chamber at 120 °C overnight and then assembled in cells similar to coin cells.[19] In each cell, a single piece of lithium metal (Aldrich, 99.9%) was used simultaneously as counter and reference electrode. It was separated from the working electrode by a 1 mm thick fiberglass separator soaked in 500 μL of electrolyte [1 M LiPF6 in ethylene carbonate (EC)/dimethyl carbonate (DMC) (1 : 1 by mass), Ferro GmbH]. Cells were assembled in an argon-filled glove box with less than 1 ppm of oxygen, water, and nitrogen contents.

Both cyclic voltammetry (CV) and rate capability experiments were performed at 25 °C by a computer-controlled cell capture (CCCC) system (Astrol Electronics AG, Oberrohrdorf, Switzerland) in a potential window of 3.5–4.5 V *vs.* Li/Li^+; the CV at a potential scan rate of 0.1 mV s^{-1}. For the rate capability experiments, the electrodes were cycled galvanostatically in the range of 3.5–4.3 V *vs.* Li/Li^+ for varying specific currents proportional to the mass of $LiMn_2O_4$. In order to promote complete discharge/charge at the respective potential limits, a potentiostatic step was included until the specific current dropped to 60 mA g^{-1}.

3. Results and discussion

The powders LMO-3/7 to LMO-8/2 were made by FSP with increasing SCE from 17.1–159.2 kJ L_{disp}^{-1}. The visible flame lengths increased from 7–30 cm, respectively. In the XRD patterns of Fig. 1, phase pure crystalline $LiMn_2O_4$ are seen for LMO-3/7 to LMO-7/3. LMO-8/2 (Fig. 1e) has about 10 wt% Mn_3O_4 and demonstrates the challenges of making pure crystalline $LiMn_2O_4$ at higher SCEs using this experimental set-up. The 9/1-flame was the SCE limit using this lab-scale reactor. The flame had a visible length of about 40 cm and a SCE of 358.2 kJ L_{disp}^{-1}. LMO-9/1 is composed of 37 wt% $LiMn_2O_4$, 38 wt% Mn_3O_4, and 25 wt% Li_2MnO_3, based on analysis of the XRD pattern (Fig. 1f). These impurities were formed during oxygen lean synthesis conditions and fast quenching promoting the formation of metastable oxides. Because of the low powder yield, no SSA and electrochemical measurements of LMO-9/1 were taken.

The crystallite size (d_{XRD}) and particle size (d_{BET}) are plotted *vs.* SCE in Fig. 2. The particle size increases with increasing SCE, reaching a maximum at 25.9 nm for LMO-8/2. In our previous work, the SSA of $LiMn_2O_4$ made by FSP were between 65 and 200 m^2 g^{-1} by varying the precursor feed rate, gas dispersion rate, and precursor molar concentration.[9] In this current work, the SCE is varied between 159.2 and 17.1 kJ L_{disp}^{-1} to produce $LiMn_2O_4$ powders with SSA between 53.9 and 203.4 m^2 g^{-1} and d_{BET} between 25.9 to 6.9 nm, respectively. The d_{BET} values were calculated assuming a particle density of 4.3 g cm^{-3}. For LMO-8/2, d_{BET} was notably higher than d_{XRD} (25.9 and 18.5 nm , respectively), suggesting this powder mixture is polycrystalline. Otherwise, the close agreement between d_{XRD} and d_{BET} indicates that single, non-aggregated, crystalline, pure $LiMn_2O_4$ nanoparticles can be produced with sizes between 6.9 and 19.4 nm by controlling SCE during flame synthesis.

Powders LMO-3/7 to LMO-8/2 were prepared into electrodes and the galvanostatic charge and discharge capacities (specific charge) measured. The average galvanostatic charge capacities of the first 5 cycles at a 0.5 C cycling rate (74 mA g^{-1}) of these electrodes are plotted in Fig. 2 against the SCE of the synthesis flames. LMO-6/4 made at 55 kJ L_{disp}^{-1} had the highest charge capacity of these results and represents the charge-capacity-optimized powder given the precursor

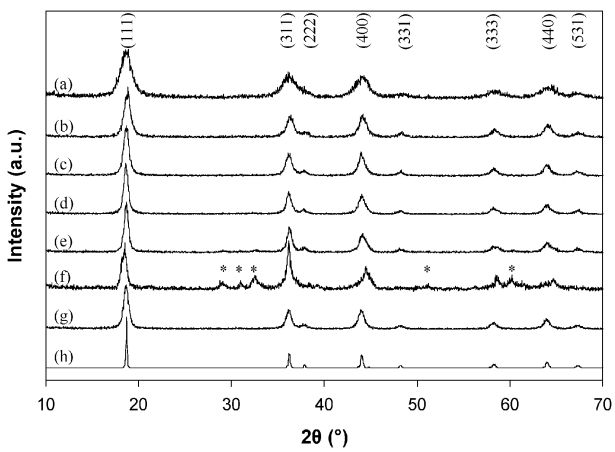

Fig. 1 XRD of $LiMn_2O_4$ powders: (a) LMO-3/7, (b) LMO-5/5, (c) LMO-6/4, (d) LMO-7/3, (e) LMO-8/2, (f) LMO-9/1, (g) LMO-6/4/10, and (h) commercial microparticles (Sigma–Aldrich). * indicates the presence of Mn_3O_4.

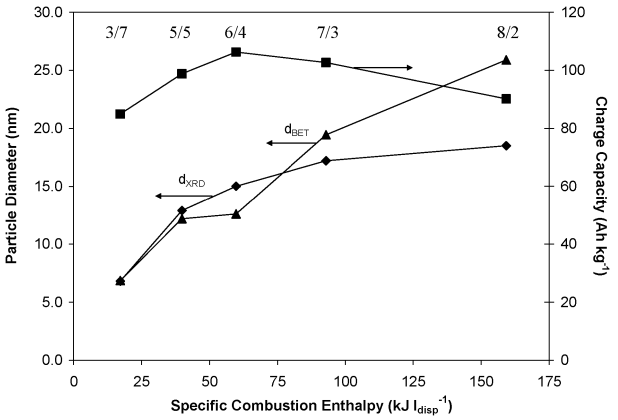

Fig. 2 Particle diameter and charge capacity (specific charge) as a function of specific combustion enthalpy. Charge capacity is calculated from the average of the first 5 galvanostatic cycles. Above the data points the corresponding precursor injection rate (mL L^{-1})/oxygen dispersion rate (L min^{-1}) is indicated.

composition and the SCE points. The impurity phase Mn_3O_4 in the powder LMO-8/2 is a contribution to its lower mass specific charge capacity. The smallest $LiMn_2O_4$ nanoparticles produced, LMO-3/7, had the lowest charge capacity of the materials tested. The measurements of LMO-3/7 in Fig. 2 were conducted at a low C-rate of 0.5 (74 mA g^{-1}), so the cause of the lower capacity is not poor electrical contact within the electrode, as this extrinsic property is only detrimental to galvanostatic charge capacity at high C-rates.[20] Consideration of the physical nature of nanoparticles leads to a better explanation. As nanoparticle diameter decreases below 20 nm, the fraction of molecules at the surface sharply increases: for model nanoparticles 20, 10, and 5 nm in diameter, the percentage of molecules at surface are 12, 25, and 50%, respectively.[21] The cause for the lower charge capacity is probably due to an increase in surface reactions corresponding with a decrease in bulk reactions. Lithium insertion to (*i.e.*, the reaction with) surface sites are known to occur at various redox potentials, as recently shown for $LiFePO_4$, where the calculated redox potentials for different surfaces range from 2.95–3.84 V, compared to the calculated potential of 3.55 V for the bulk.[22] Therefore, the electrochemical potentials for lithium incorporation into surface vacancy sites are different than lithium incorporation into bulk vacancy sites. As nanoparticles decrease below 20 nm, the fraction of surface sites increases and the fraction of bulk sites decreases. Surface molecules may possess a smaller density of lithium vacancy sites, leading to a decrease in charge capacity as seen with TiO_2 nanoparticles smaller than 10 nm and also with $LiCoO_2$ nanoparticles smaller than 15 nm.[23,24] Therefore, the decrease in specific charge and discharge capacities of the $LiMn_2O_4$ nanoparticles below d_{XRD} of 15 nm is attributed to the decrease in the fraction of lithium vacancy sites in the bulk.

To investigate the above hypothesis, electrochemical behaviour was studied using cyclic voltammograms (CVs). The CVs of the LMO-6/4 and LMO-3/7 electrodes are illustrated in Fig. 3a and b, respectively. The oxidative peaks in the 1st cycle are at 4.04 and 4.17 V and the reductive peaks at 3.95 and 4.07 V, which are consistent with literature[9,25,26] and also the same position as the CV of the commercial microparticles (Fig. 3d). These CVs are similar in peak position, but are different in shape: the peaks are better defined in Fig. 3a (d_{XRD} = 15.0 nm) than in Fig. 3b (d_{XRD} = 6.8 nm). The profile differences are illustrated in Fig. 4, where % normalized capacity stored in regions 3.5–3.9 V and 4.2–4.5 V increases as d_{XRD} decreases. LMO-3/7 (d_{XRD} = 6.8 nm) has a higher % normalized capacity in these potential ranges than the larger LMO-6/4 nanoparticles (d_{XRD} = 15.0 nm). Lithium incorporation into surface vacancy sites occurs over a range of electrochemical potentials, as seen in $LiFePO_4$.[22] The number of surface vacancy sites per unit mass is greater for LMO-3/7 (SSA = 203.4 m^2 g^{-1}) than for LMO-6/4 (SSA = 110.7 m^2 g^{-1}). The surface and bulk redox potentials all contribute to the CVs in Fig. 3, but the contribution of surface redox potentials is most apparent in the CV of the smaller $LiMn_2O_4$ nanoparticles (Fig. 3b). The lower charge capacity of LMO-3/7 (Table 1 and Fig. 2) is likely due to a decrease of charge storage at the bulk redox potentials measured by the CV experiments.

In a variation of synthesis conditions, a 10 L min^{-1} of oxygen sheath gas was used during production with a 6/4-flame to make the powder LMO-6/4/10. The oxygen sheath gas is expected to increase the quench rate of the nanoparticles as has been seen in literature.[27] The 6/4/10-flame was 15 cm in length, the same visible length as the 6/4-flame. With SSA, d_{BET}, and d_{XRD} of 97.8 m^2 g^{-1}, 14.3 nm, and 16.6 nm, respectively, LMO-6/4/10 is composed of single, crystalline particles about 10% larger (d_{XRD}) than LMO-6/4. There are no detectable differences in the XRD pattern for powders produced with and without sheath gas (Fig. 1c and g) and therefore the powders have similar bulk crystallinity. Yet, analysis of the CVs of LMO-6/4 and LMO-6/4/10 in the 1st cycle (Fig. 3a and c) suggests there could be some structural difference. For the CV of LMO-6/4/10, there are 3 oxidative peaks at 4.07, 4.17, and 4.24 V and 3 reductive peaks at 3.84, 3.96, and 4.08 V. The 3rd peaks seen in the CV of LMO-6/4/10 are not seen in the 5th and 20th cycle. The electrochemical over potentials in the 1st cycle indicate that there is a kinetic barrier to lithium extraction/insertion from/into the spinel structures in the bulk of LMO-6/4/10. In the 1st cycle, the surface of LMO-6/4/10 limits lithium transport to the lithium vacancy sites in the bulk. We suggest that the surface structures of LMO-6/4/10 are initially less crystalline or defective or both due to quenching by the O_2 sheath gas during synthesis. In the 5th and 20th cycle, the CVs of LMO-6/4/10 and LMO-6/4 resemble each other, suggesting that the surface of LMO-6/4/10 has become thermodynamically stable. In Fig. 4, the plot of lithium extraction from LMO-6/4/10 closely resembles that of LMO-6/4 in the potential regions negative to 3.9 V and also positive to 4.3 V. In the 3.9–4.3 V region, there is little distinction between the two plateaus of the plot of LMO-6/4/10 and LMO-6/4. This is an indication that a portion of the LMO-6/4/10 material is not fully crystalline,[28] even though the bulk of the nanoparticles are (Fig. 1g). Synthesis by FSP produces oxides in one-step because of the high temperatures (>2000 °C) and rapid cooling, as has been measured by Fourier transform infrared spectroscopy during the synthesis of Pt/TiO_2.[27] Use of the O_2 sheath gas in

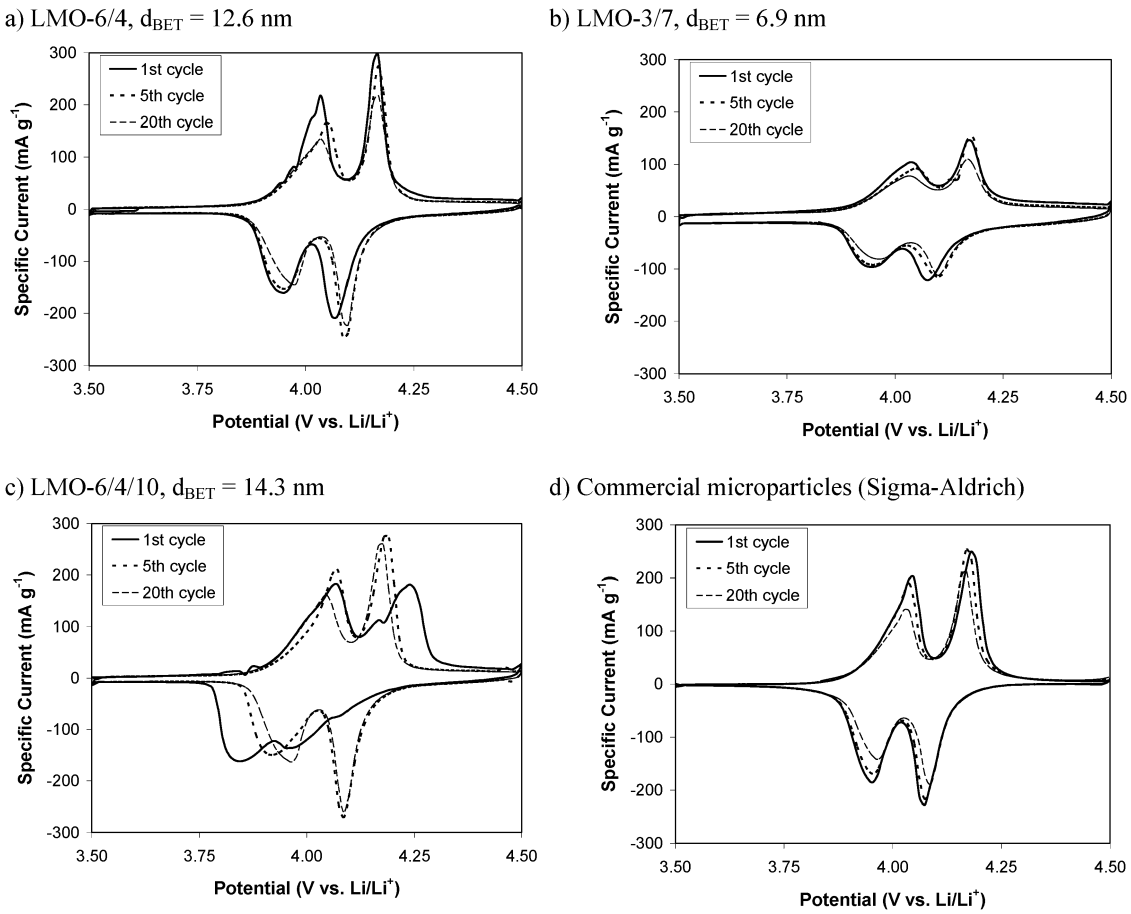

Fig. 3 Cyclic voltammograms of $LiMn_2O_4$ powders in the 1st, 5th, and 20th cycle at 0.1 mV s^{-1}.

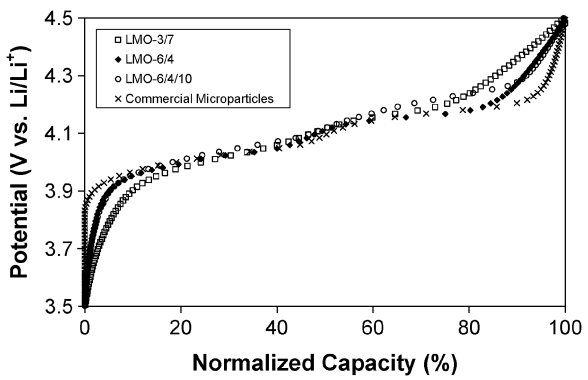

Fig. 4 Voltammetric charging (delithiation) at 0.1 mV s^{-1} of $LiMn_2O_4$ samples. These plots are based on the 1st charge of the cyclic voltammograms presented in Fig. 3. Normalized capacity is the capacity expressed as a % of the total capacity.

the 6/4/10-flame increased the quenching rate, likely cooling the material more rapidly than for the 6/4-flame, creating surface structures less crystalline or more defective than the bulk. Although the SCE is by definition the same for both the 6/4- and the 6/4/10-flame, the difference in electrochemistry of the resulting powders is an indication of the difference in synthesis conditions. The distribution of enthalpy throughout the flame likely led to the variation in size and crystallinity. High resolution TEM investigations of LMO-6/4 and LMO-6/4/10 could provide visual evidence of the difference in surface structures and are planned for upcoming investigations.

Rate capability experiments of selected as-made $LiMn_2O_4$ nanoparticles are seen in Fig. 5. LMO-6/4/10 (d_{XRD} = 16.6 nm) has the highest capacity between 0.5 and 10 C, indicating that the non-thermodynamically stable surface structures are not necessarily a detrimental factor to charge and discharge capacity, so long as there is a sufficient amount of crystalline bulk. At 20 C, LMO-6/4 (d_{XRD} = 15.0 nm) has the higher specific charge capacity, likely because of the smaller size which leads to improved charge transfer and smaller diffusion path lengths to active sites. The powder LMO-6/4 retained a galvanostatic discharge capacity at 50 C over 80 mAh g^{-1} beyond 60 cycles. In combination with the co-synthesis of carbon black, flame-produced $LiMn_2O_4$ nanoparticles could be a potential replacement to supercapacitors in high power applications.[10] The trend of higher SSA leading to improved charge/discharge capacity does not continue within the range of current densities tested. Although smaller in size, LMO-5/5 (d_{XRD} = 12.9 nm) and LMO-3/7 (d_{XRD} = 6.8 nm) have lower charge and discharge capacities. This trend is also seen in the work of Okubo *et al.*: a range of $LiCoO_2$ nanoparticles were tested and it was concluded that size reduction below 15 nm was not favorable for most applications.[24] For the $LiMn_2O_4$ nanoparticles tested in our work, d_{XRD} of 15 nm seems to be an appropriate, approximate limit, below which electrochemical performance is less favourable. $LiMn_2O_4$ nanoparticles less than 15 nm are attractive for the improved diffusion and charge transfer

Table 1 Summary of material properties and specific charge/discharge capacities of as-prepared powders. Specific charge/discharge capacities are calculated from the average of the first 5 galvanostatic cycles

Sample	BET SSA $m^2\ g^{-1}$	d_{BET} nm	d_{XRD} nm	Specific enthalpy kJ L_{disp}^{-1}	Specific charge capacity Ah kg^{-1}	Specific discharge capacity Ah kg^{-1}
LMO-3/7	203.4	6.9	6.8	17.1	84.9	80.4
LMO-5/5	114.5	12.2	12.9	39.8	98.8	94.6
LMO-6/4	110.8	12.6	15.0	59.7	106.3	102.4
LMO-7/3	71.8	19.4	17.2	92.9	102.7	96.1
LMO-8/2	53.9	25.9	18.5	159.2	90.2	86.4
LMO-6/4/10[d]	97.8	14.3	16.6	59.7	113.3	107.2

[a] BET equivalent particle diameter, $d_{BET} = 6(\rho^*SSA)^{-1}$. [b] Enthalpy of liquid in kJ min^{-1} divided by dispersion gas flow rate in $L_{disp}\ min^{-1}$. [c] Average of first 5 cycles at 0.5 C. [d] A O_2 sheath gas of 10 L min^{-1} used during production.

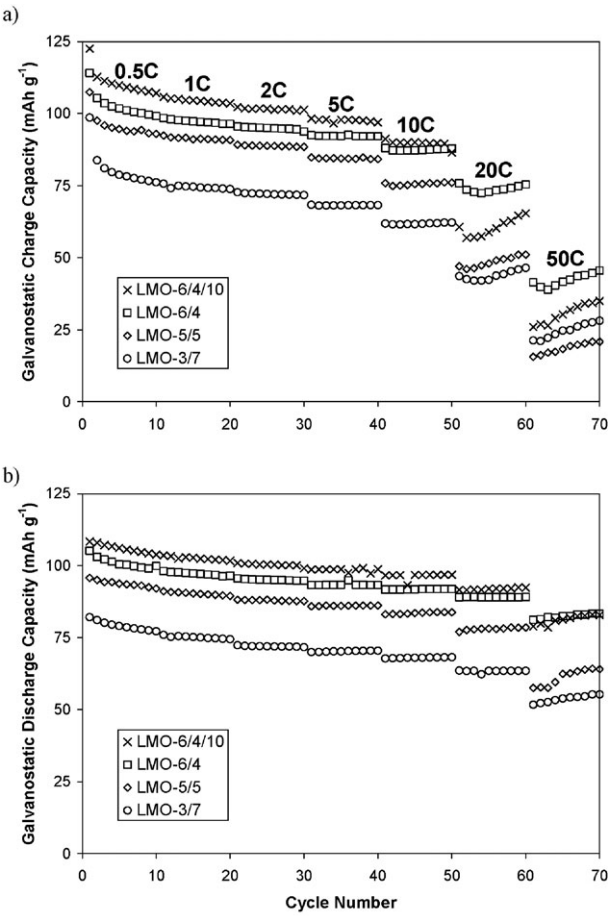

Fig. 5 Galvanostatic lithium–ion extraction (charge, a) and insertion (discharge, b) capacities for electrodes with the FSP-produced $LiMn_2O_4$ nanoparticles at increasing C-rates with cut-off potentials of 3.5 and 4.3 V *vs.* Li/Li^+. Here 1 C is set to 148 A kg^{-1}. C-rates and capacities are based on the mass of $LiMn_2O_4$ in the electrode. Only the galvanostatic part of the respective cycle is considered here.

properties, but the smaller fraction of lithium vacancy sites in the crystalline bulk decreases charge capacity for electrochemical energy storage.

4. Conclusions

In this work, production of $LiMn_2O_4$ by FSP in a single step is demonstrated to be a route to control nanoparticle size by control of specific combustion enthalpy. FSP can be used for rational design of single $LiMn_2O_4$ nanoparticles for high power Li–ion batteries. The electrochemical performances of flame-made particles between 7 and 25 nm were measured. The powder with optimized d_{XRD} of 15 nm retained a galvanostatic discharge capacity at 50 C of over 80 mAh g^{-1} beyond 60 cycles. Furthermore, enthalpy distribution throughout the flame was modified by an oxygen sheath gas during synthesis. This modification had a direct impact on modifying the surface structure as measured by cyclic voltammetry. For the best rate capability performance, crystalline $LiMn_2O_4$ nanoparticles with d_{XRD} greater than 15 nm are essential. Smaller sizes lack crystalline bulk and the advantages of improved charge transfer and smaller diffusion path lengths do not improve performance for specific currents between 0.5 and 50 C.

Acknowledgements

Continuous support from and scientific discussions with Prof. S. E. Pratsinis (ETH Zurich) and Prof. A. Wokaun (PSI and ETH Zurich) are greatly appreciated. Technical assistance of Mr W. Scheifele (PSI) and Mr H. Kaiser (PSI) is highly appreciated. This research was partially funded by the ETH Research Grant TH-29/05-2 and TH-09/06-2 (R. Büchel). T. J. Patey thanks the ETH Zurich/Tokyo Tech exchange scholarship program for partial financial support.

References

1 P. J. Hall and E. J. Bain, *Energy Policy*, 2008, **36**, 4352–4355.
2 M. M. Thackeray, P. J. Johnson, L. A. de Picciotto, P. G. Bruce and J. B. Goodenough, *Mater. Res. Bull.*, 1984, **19**, 179–187.
3 R. J. Gummow, A. Dekock and M. M. Thackeray, *Solid State Ionics*, 1994, **69**, 59–67.
4 M. Winter, J. O. Besenhard, M. E. Spahr and P. Novak, *Adv. Mater.*, 1998, **10**, 725–763.
5 M. Lanz, C. Kormann, H. Steininger, G. Heil, O. Haas and P. Novák, *J. Electrochem. Soc.*, 2000, **147**, 3997–4000.
6 A. S. Arico, P. Bruce, B. Scrosati, J. M. Tarascon and W. van Schalkwijk, *Nat. Mater.*, 2005, **4**, 366–377.
7 K. M. Shaju and P. G. Bruce, *Chem. Mater.*, 2008, **20**, 5557–5562.
8 C. J. Curtis, J. X. Wang and D. L. Schulz, *J. Electrochem. Soc.*, 2004, **151**, A590–A598.
9 F. O. Ernst, H. K. Kammler, A. Roessler, S. E. Pratsinis, W. J. Stark, J. Ufheil and P. Novák, *Mater. Chem. Phys.*, 2007, **101**, 372–378.
10 T. J. Patey, R. Büchel, S. H. Ng, F. Krumeich, S. E. Pratsinis and P. Novák, *J. Power Sources*, 2009, DOI: 10.1016/j.jpowsour.2008.10.002.

11 H. D. Jang, C. M. Seong, Y. J. Suh, H. C. Kim and C. K. Lee, *Aerosol Sci. Technol*., 2004, **38**, 1027–1032.
12 T. J. Patey, S. H. Ng, R. Buechel, N. Tran, F. Krumeich, J. Wang, H. K. Liu and P. Novák, *Electrochem. Solid-State Lett*., 2008, **11**, A47–A50.
13 A. Camenzind, R. Strobel and S. E. Pratsinis, *Chem. Phys. Lett*., 2005, **415**, 193–197.
14 L. Mädler, H. K. Kammler, R. Mueller and S. E. Pratsinis, *J. Aerosol Sci*., 2002, **33**, 369–389.
15 L. Mädler, W. J. Stark and S. E. Pratsinis, *J. Mater. Res*., 2002, **17**, 1356.
16 R. Strobel and S. E. Pratsinis, *J. Mater. Chem*., 2007, **17**, 4743–4756.
17 S. Brunauer, P. H. Emmett and E. Teller, *J. Am. Chem. Soc*., 1938, **60**, 309–319.
18 R. W. Cheary and A. Coelho, *J. Appl. Crystallogr*., 1992, **25**, 109–121.
19 P. Novák, W. Scheifele, F. Joho and O. Haas, *J. Electrochem. Soc*., 1995, **142**, 2544–2550.
20 T. J. Patey, A. Hintennach, F. La Mantia and P. Novák, *J. Power Sources*, 2009, DOI: 10.1016/j.jpowsour.2008.09.091.
21 O. Preining, *J. Aerosol Sci*., 1998, **29**, 481–495.
22 L. Wang, F. Zhou, Y. S. Meng and G. Ceder, *Phys. Rev. B: Condens. Matter Mater. Phys*., 2007, **76**, 165435.
23 J. Wang, J. Polleux, J. Lim and B. Dunn, *J. Phys. Chem. C*, 2007, **111**, 14925–14931.
24 M. Okubo, E. Hosono, J. Kim, M. Enomoto, N. Kojima, T. Kudo, H. S. Zhou and I. Honma, *J. Am. Chem. Soc*., 2007, **129**, 7444–7452.
25 Y. Y. Xia and M. Yoshio, *J. Electrochem. Soc*., 1996, **143**, 825–833.
26 W. Liu, G. C. Farrington, F. Chaput and B. Dunn, *J. Electrochem. Soc*., 1996, **143**, 879–884.
27 H. Schulz, L. Mädler, R. Strobel, R. Jossen, S. E. Pratsinis and T. Johannessen, *J. Mater. Res*., 2005, **20**, 2568–2577.
28 T. Tsumura, A. Shimizu and M. Inagaki, *Solid State Ionics*, 1996, **90**, 197–200.